Gyro-Multigrid Triboelectric Nanogenerator via Topological Defects Strategy for Efficiently Harvesting Low-Grade Wave Energy

Wei Gao, Xiaobo Gao, Juan Su, Huisheng Cai, Hao Li, Baodong Chen, and Zhong Lin Wang**

Wave energy is a promising sustainable energy yet to be fully exploited due to the low frequency and broad-banded wave fields, so much so that difficult to capture, resulting in low efficiency and limited power output from current many wave energy harvesters. Here, a topological defect gyro-multigrid triboelectric nanogenerator (TD-GM-TENG) is proposed that harnesses the mechanical energy of ocean waves to generate electricity and promotes the accumulation of triboelectric charge on the basis of realized from low to high rotation speed under the precession and gravitation acceleration effects. It benefited from topological defect strategy, TD-GM-TENG offers a charge transfer rate of 3.1 μC s^{-1} that when can reach to a speed of nearly 1000 rpm at the wave frequency of 1 Hz. Furthermore, the charge density reaches 90 μC m^{-2} in a cycle of 0.06 s, which is 1.6 times higher than the same kind of spherical-TENGs in the field of ocean energy harvesting. Finally, TD-GM-TENG unit outputs a peak power of 3.7 mW at the simulated water wave environment of 1 Hz and demonstrates its applicability and feasibility of being used as a distributed emergency power supply in the offshoring observation and early warning services.

1. Introduction

Wave energy is a sustainable energy source that is generated by the movement of ocean waves created by the wind blowing across its surface. As a green, inexhaustible, and largely untapped resource, it is very important to do converting the mechanical energy produced by ocean waves into electricity by energy harvesting technologies. So that, it has the potential to play a key role in the global transition toward sustainable energy systems. With the rise of the adolescent offshore industry like Internet of Things,[1] ocean security, ocean climatic, and ocean economy. In the past for a long time, advanced information and communication technologies have been applied to the development of various ocean emergency and observation platforms. The power supply problem brought by a large number of electron devices and sensors applications is becoming the increasingly prominent and severe. Meanwhile, the advanced harvesting technology of the wave energy has attracted more and more attention in the context of the global focus on achieving carbon peak and carbon neutrality.[2]

Triboelectric nanogenerators (TENGs) have emerged as a promising solution for large-scale ocean wave energy harvesting.[3] TENGs effectively convert the mechanical energy produced by ocean waves into electricity, making them particularly adept at capturing low-frequency energy, which opens new possibilities for harvesting technology.[4–10] The operation of TENGs relies on the triboelectric effect, where the contact and separation of two materials with different electron affinities cause electrons to transfer between them. When these materials come into contact, electrons move from the material with a lower electron affinity to the one with a higher affinity. Upon separation, a potential difference is created, generating electrical voltage and enabling the flow of charge.[11–14] Enhancing the conversion efficiency of ocean wave energy utilization is crucial, given the vast energy reserves the ocean offers. Among the various fluctuation characteristics of the ocean waves, the irregular wave is particularly promising, which occupies the major proportion in all ocean waves.[15–17] Traditional electromagnetic generators, however, struggle with generation principles, operating conditions, material selection, and complex designs, making them less effective at capturing the small-scale, irregular energy of ocean waves.[18] In contrast, TENG offers a simpler, low costs, high conversion efficiency, and broad applicability in the face of all-fluctuation range of ocean wave energy harvesting.[19–25] The high adaptability and adjustability of their structures are well-suited for use in over large oceanic areas, and the working

W. Gao, X. Gao, H. Li, B. Chen, Z. L. Wang
Beijing Institute of Nanoenergy and Nanosystems
Chinese Academy of Sciences
Beijing 101400, P. R. China
E-mail: chenbaodong@binn.cas.cn; zlwang@gatech.edu

W. Gao, J. Su, H. Cai, B. Chen
School of Materials Science and Engineering
Inner Mongolia University of Technology
Hohhot 010051, P. R. China

X. Gao, H. Li, B. Chen, Z. L. Wang
School of Nanoscience and Engineering
University of Chinese Academy of Sciences
Beijing 100049, P. R. China

DOI: 10.1002/aenm.202405398

principle making them especially suited for harvesting the irregular and micro-nano fragmentized energy of ocean waves.[26–35] Over the past decade, multitudinous TENGs just keep emerging, there can be no doubt that TENG development has progressed rapidly, from the fundamental physical theory understanding to improved performances and extended applications. We have recognized that the surface charge density as one of the key factors to improve the output of TENGs, has been widely studied, but the controlling and modulating of the charge density is far from satisfactory. How to break through the bottleneck of electrical output performance by the wat of improving charge accumulation has always been a hot topic in this field.

On the basis of the present situation of the latest research of triboelectric charge accumulation,[36–39] a topological defect gyro-multigrid triboelectric nanogenerator (TD-GM-TENG) is proposed here, which harnesses the low-grade broken mechanical energy of ocean waves to generate electrical energy by regulating the oscillation frequency and resonance effect. It benefited from the introduction of topological defect and gyro-multigrid structure, the process of charge accumulation is changed by the structure defect of the gate triboelectric layer and improved the efficiency of charge accumulation on the basis of realized from low to high rotation speed under the precession and gravitation acceleration effects. Compared with previous studies,[40–44] the charge density in a single cycle is greatly improved, which reached 90 μC m^{-2} in a cycle of 0.06 s, which is 1.6 times higher than the same kind of spherical-TENGs in the field of ocean energy harvesting. The peak power of a TD-GM-TENG unit reached 3.7 mW at the simulated water wave environment of 1 Hz, a distributed emergency power supply system was integrated by TD-GM-TENG array and demonstrates its applicability and feasibility in the offshoring observation and early warning services.

2. Results and Discussion

Figure 1a shows the exploded view of TD-GM-TENG, which consists of four main components: a support frame equipped with a unidirectional rotating bearing, a rotor, a 3D printed resin housing (stator), and a waterproof housing. The rotor is evenly distributed with grid fur, and the nano silver electrode layer and fluorinated ethylene propylene (FEP) film are at the bottom of the resin shell (Figure S1, Supporting Information). The reason why TD-GM-TENG generates a potential difference is that the contact area changes during rotation, thereby changing the induced charge between the electrodes (Figure 1b,c). The photo of TD-GM-TENG is shown in Figure 1d. Figure 1e illustrates the operating principal diagram of TD-GM-TENG. In the first stage, TD-GM-TENG needs to overcome a large friction force (static friction is converted into sliding friction), so the initial wave height is relatively high. In the second stage, the increase in speed causes TD-GM-TENG to have a precession effect, and the energy required for rotation begins to decrease (only sliding friction is overcome). In the third stage, the speed begins to increase further. Due to the precession effect, TD-GM-TENG maintains a high speed in this stage. In the fourth stage, the acceleration process ends, and the speed will drop slightly due to the friction resistance of TD-GM-TENG itself. The output performance of TD-GM-TENG is shown in Figure 1f and Figure S2 (Supporting Information), with a short-circuit current of 4 μA and a transferred charge of 140 nC (In order to facilitate subsequent performance comparison, the data in this article are processed with the same coordinate scale).

Experiments have found that charge will accumulate significantly after the speed increases. Therefore, the conductive copper sheet is introduced as a defect structure to improve the efficiency of charge utilization (Figure 1g). In structured grid-like fur, the fur continuously supplies charges to the FEP. However, in practice, a portion of these charges remains trapped on the FEP and does not contribute to the electrostatic induction, significantly reducing the charge utilization efficiency of the TENG. To address this issue, a defect structure is introduced to disrupt the charge accumulation process, facilitating directional discharge that releases the accumulated charges on the FEP before harmful discharge occurs, thereby enhancing the overall charge utilization efficiency. It can be found that the transfer charge has changed significantly after the defect structure was introduced. Increasing the width of the defect structure and reducing the height will increase the transferred charge, but since the accumulated charge remains unchanged, the transfer charge has a maximum value. Reducing the height of the defect structure will reduce the air breakdown voltage and improve the charge release efficiency (Figure 1h,i; Figure S3, Supporting Information). As the width of the copper electrode increases further, the transferred charge does not exhibit a corresponding enhancement. This is attributed to the fact that there is a maximum charge accumulation within a single operational cycle of the triboelectric nanogenerator (TENG). The role of the copper electrode's width is to expand the area available for charge release. However, experimental observations reveal that the accumulated charge is not uniformly distributed across the surface of the FEP film. Typically, one side of the FEP accumulates more charge than the other. This asymmetry is further supported by COMSOL simulations. Consequently, after the width of the copper electrode reaches a certain value, most of the charges have been released, and if the width continues to increase, the accumulated charge will not increase, so the transferred charge tends to be stable as the width increases.

Figure 2a is a schematic diagram of the two structures (GM-TENG and TD-GM-TENG), and the role of the topological defect structure in the charge transfer process is shown in Figure 2b. Under simulation conditions, the removal of the fur will cause the charge to disappear. However, actual tests show that only a portion of the generated charge disappears, while the other portion accumulates on the FEP and does not participate in electrostatic induction. The defect structure can effectively avoid this situation. The accumulated negative charge is released by breaking through the air, while the number of positive charges on the fur remains unchanged. At this time, the number of electrostatically induced charges has increased significantly. The potential simulation of TD-GM-TENG was carried out, and it was found that the introduction of the defect structure effectively changed the potential distribution and promoted the charge transfer (Figure 2c). Figure 2d is the equivalent circuit diagram of the defect-free structure and the defective structure. FEP is equivalent to a capacitor C_{FEP}. However, C_{FEP} has a large capacitive reactance, most of the charge will accumulate at C_{FEP}, and only a small amount of charge will pass through C_{FEP}. In the equivalent circuit of the defective structure, air and FEP can be regarded as capacitor C_1, and the parallel connection of breakdown diode D_2 and resistor R_2. The accumulated charge only needs a lower voltage to break down

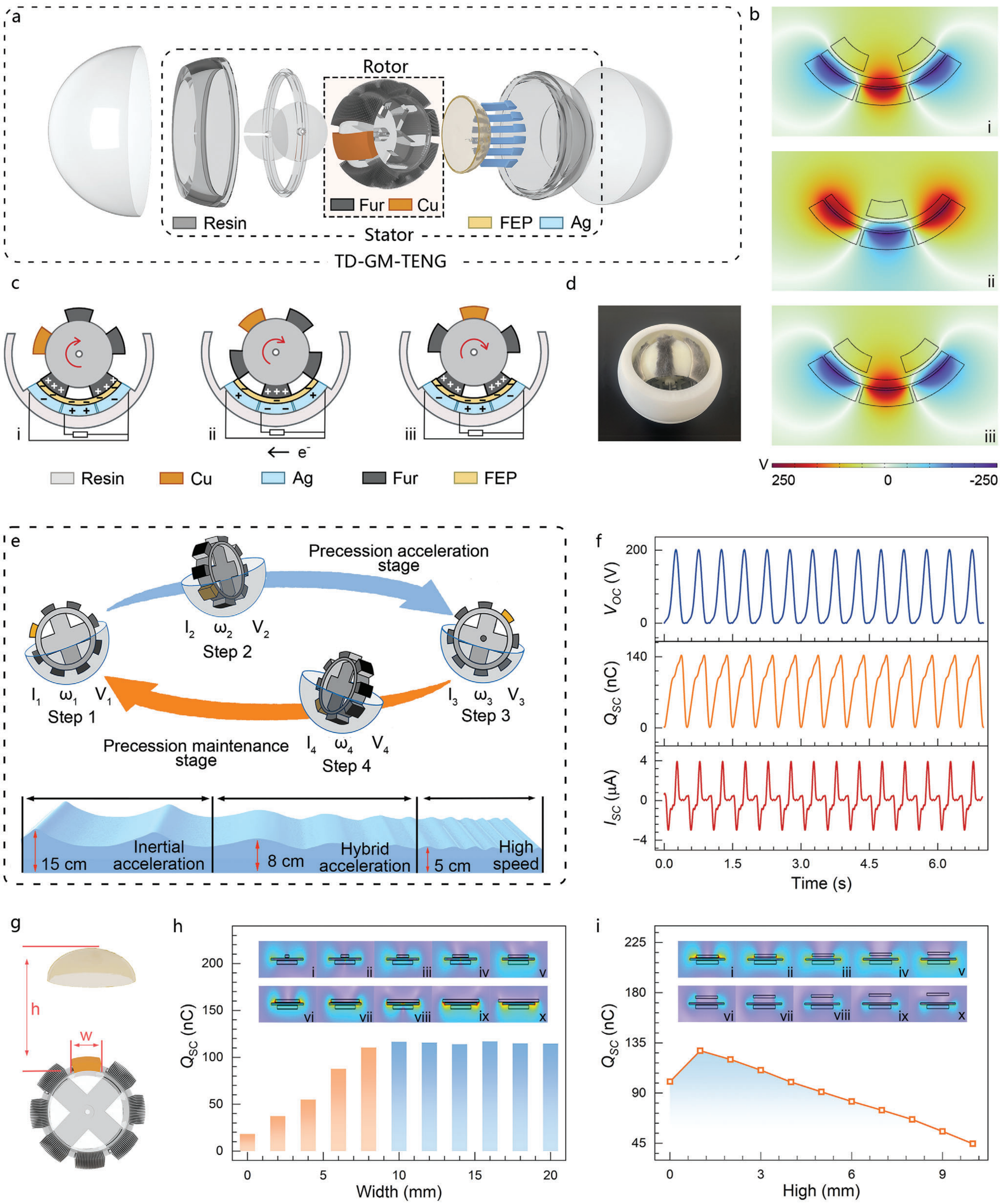

Figure 1. Structure, principle, and electrical output characteristic of topological defect gyro-multigrid triboelectric nanogenerator (TD-GM-TENG). a) Structure exploded diagram of TD-GM-TENG. b) Potential distribution simulation of TD-GM-TENG by COMSOL soft. c) Working principle of TD-GM-TENG. d) Physical photo of TD-GM-TENG. e) Operating principal diagram of TD-GM-TENG. f) Electrical output characteristic of TD-GM-TENG. g) Schematic diagram of copper sheet width and spacing of TD-GM-TENG. h) Effect of copper electrode width on transferred charge. i) Effect of the distance between copper electrode and film on transferred charge.

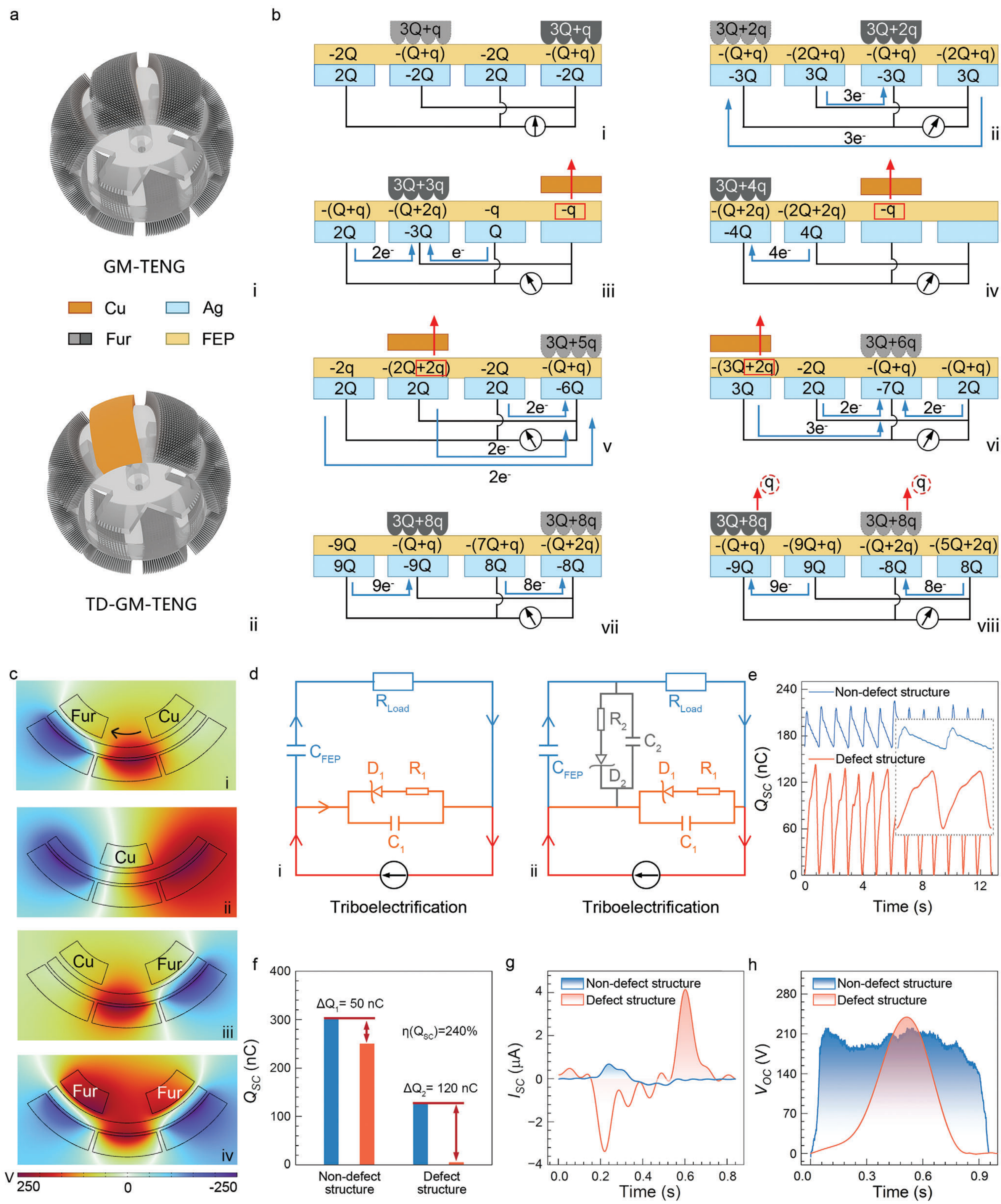

Figure 2. Fundamental physics properties and output performance of TD-GM-TENG. a) Comparative schematic diagram of GM-TENG and TD-GM-TENG. b) Charge transfer process of TD-GM-TENG with topological defect realized by copper electrode. c) Potential simulation diagram of TD-GM-TENG. d) Equivalent circuit diagram of topological defect structure from TD-GM-TENG. e) Comparative transferred charge of TD-GM-TENG with and without topological defect. f) Comparative number of transferred charge with and without topological defect. g) Comparative waveforms of short-circuit current with and without topological defect. h) Comparative waveforms of open-circuit voltage with and without topological defect.

D_2, thereby achieving the purpose of reducing the accumulated charge and improving the charge utilization efficiency. Figure 2e is the waveform of the transferred charge. The appearance of the defect structure changes the peak value of the transferred charge, causing the accumulated charge to be released quickly. By calculating the transferred charge, it can be found that the ΔQ_1 of the defect-free structure is 50 nC, while the ΔQ_2 of the defective structure reaches 120 nC, and the charge utilization efficiency is improved by 240% (Figure 2f). After adding the defective structure, the waveforms of the short-circuit current and open-circuit voltage have changed significantly. Due to the short discharge time of the defective structure, the short-circuit current is significantly increased (Figure 2g,h), and the open-circuit voltage has changed from the previous wide peak to a narrow peak. Based on this characteristic, the topological defect strategy can be used in rotary TENGs with electrostatic breakdown. It can effectively curb harmful discharges between triboelectric layers, reduce the number of charges that do not participate in electrostatic induction, and thus increase the charge utilization efficiency.

Precession refers to the phenomenon where the gyroscopic rotor experiences a shift in the horizontal plane, resulting in a change in its angular momentum. Under the combined influence of the conservation of angular momentum and the precession effect, the TENG undergoes rotational motion. This leads to a significant increase in rotational speed, thereby greatly enhancing the charge transfer rate (**Figure 3**a). Among them, the precession torque is the main factor. This is because the precession torque will change the precession angle of TD-GM-TENG. The relationship between precession torques, precession angle and rotation speed are shown in Figure 3b. When TD-GM-TENG rotates, the axis of rotation is deflected upward and downward due to the gravitational torque (*M*) acting on it. This action generates incremental angular momentum (*dL*) along the axis of rotation. The newly generated *dL* can be expressed in terms of moment of inertia (*I*) and angular velocity (*ω*), so the state of TD-GM-TENG can be described as follows:

$$dL = -I\omega \sin\theta d\theta \tag{1}$$

TD-GM-TENG generates a precession effect on this plane to maintain its overall angular momentum. Therefore, the faster the rotation speed increases, the faster its moment of inertia and angular velocity increases. According to the precession effect formula:

$$\widehat{H} = \begin{bmatrix} I_1\omega_1 \\ I_2\omega_2 \\ I_3\omega_3 \end{bmatrix} \tag{2}$$

Among them, I_1, ω_1, I_2, ω_2, I_3, and ω_3 are the moment of inertia and angular velocity of TD-GM-TENG in the *x*-axis, *y*-axis, and *z*-axis, respectively. Where θ is the precession angle, which can be expressed as:

$$\begin{cases} \widehat{\psi} = -H\left(\frac{\sin^2\phi}{I_2} + \frac{\cos^2\phi}{I_3}\right) \\ \widehat{\theta} = \frac{H}{2}\left(\frac{1}{I_3} - \frac{1}{I_2}\right)\sin 2\phi\cos\theta \\ \widehat{\varphi} = H\left(\frac{1}{I_1} - \frac{\sin^2\phi}{I_2} - \frac{\cos^2\phi}{I_3}\right)\sin\theta \end{cases} \tag{3}$$

And $\widehat{\psi}$, $\widehat{\theta}$ and $\widehat{\varphi}$ are the components of the precession effect in the x, y, and z planes, respectively. As the moment of inertia and angular velocity increases, the precession angle θ also increases. Comparing the rotation speed with and without the precession effect, TD-GM-TENG without precession only has inertial rotation, while TD-GM-TENG with precession has two acceleration stages (inertial acceleration and angular momentum acceleration), in which the rotation speed is three times that of inertial rotation (Figure 3c).

From the force analysis of TD-GM-TENG, the angular momentum of the wave becomes greater than that of TD-GM-TENG, which will cause friction between the stator and the two ends of the shaft. In the acceleration stage, the direction of the friction force is opposite to the direction of movement of the shaft, which combines with the deflection force generated by the precession effect to provide additional driving force for TD-GM-TENG (Figure S4a,b, Supporting Information). When the acceleration stage ends, the angular momentum of TD-GM-TENG is equal to the angular momentum of the wave, the friction force generated by the shell track is consistent with the rotation direction of the shaft, and the force component generated by the precession effect offsets this friction force. The force conditions at both ends of the rotor shaft at this stage are shown in Figure S4c (Supporting Information). Finally, as shown in Figure S4d (Supporting Information), TD-GM-TENG returns to the initial state (the motion photo of TD-GM-TENG is shown in Figure S5, Supporting Information). Therefore, the speed and output characteristics of TD-GM-TENG change at different stages. Figure 3d shows the transferred charge of TD-GM-TENG at different angles, and the output performance is different at different stages. Figure 3e also shows the force conditions at both ends of the rotating shaft at different stages, which further verifies this point. Under the same counterweight, the larger the rotor diameter of TD-GM-TENG, the faster the speed. Figure 3f illustrates the impact of the added mass and rotor diameter on the rotational speed of TD-GM-TENG under fixed wave height (10 cm) and frequency (1 Hz) for the simulated waves. Both the added mass and rotor diameter effectively enhance the rotational speed of the TD-GM-TENG. According to the equation $I = mr^2$, increasing either the added mass or the rotor diameter increases the rotational inertia of the system, thereby boosting the rotational speed. For the TENG without precession effect, when the height and frequency of the wave are stable, there is only inertial rotation, and the rotation speed is much lower than that of the TENG with precession effect. Figure 3g shows the change process of the short-circuit current of TD-GM-TENG in different acceleration states. In the inertial acceleration and angular momentum acceleration stages, the short-circuit current has increased significantly compared with before, which is caused by the increase in speed. The horizontal rotation of TD-GM-TENG is an acceleration cycle, so the faster the horizontal movement speed, the higher the speed that the internal energy can reach. However, due to the resonance phenomenon, when the acceleration frequency is too high, the maximum speed will be limited (Figure 3h). Based on the different rotation characteristics of TD-GM-TENG, the angle between the fur and the electrode will change, which will also affect the output performance. When the angle is 0°, the output performance is reduced by 20% (Figure 3i). The short-circuit current of

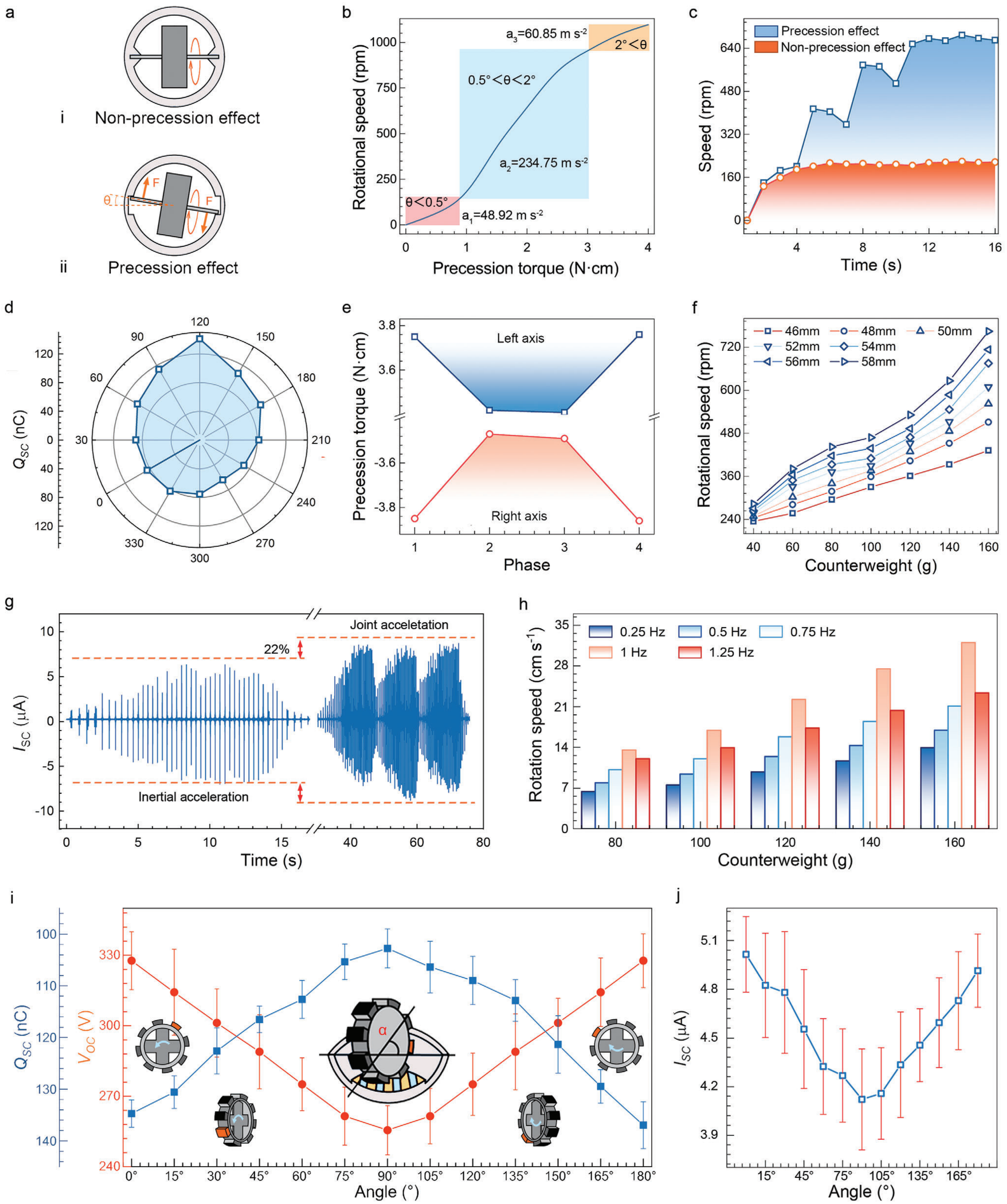

Figure 3. Electrical output performance of TD-GM-TENG with different gyro-multigrid parameters. a) Comparison schematic diagram of the precession and gravitation acceleration effects of TD-GM-TENG. b) The relationship between the rotational speed and precession torque. c) The relationship between precession effect and rotation speed. d) The relationship between TD-GM-TENG motion angle and transferred charge. e) The relationship between the precession torques at both ends of the shaft. f) Effect of counterweight and diameter of TD-GM-TENG on rotation speed. g) Short-circuit current variation relationship at different acceleration stages. h) Effect of counterweight and motion frequency of TD-GM-TENG on horizontal rotation speed. i) Output performance of TD-GM-TENG at different horizontal angles. j) Short-circuit current of TD-GM-TENG at different horizontal angles.

TD-GM-TENG at different angles also conforms to this characteristic (Figure 3j).

To achieve higher rotational speeds, the TD-GM-TENG employs a soft contact approach. As the fur serves as the soft contact material, its mechanical properties significantly influence the durability of the TENG. Therefore, in preliminary experiments aimed at identifying fur with optimal mechanical properties, we tested various types of fur, including Angora rabbit fur, New Zealand rabbit fur, French rabbit fur, and Chinese rabbit fur. Among these, Angora rabbit fur (underfur) exhibited high resistance and low stiffness, resulting in ineffective contact. In contrast, French rabbit fur (long guard fur, which is easier to control in length) provided better contact due to its inherent stiffness and thus was selected for use in subsequent experiments (Table S1, Supporting Information). In addition to the mechanical properties of fur, the structural factors of fur also affect the output performance. When the length of the fur increases from 10 to 30 mm, the open circuit voltage decreases from about 280 to 100 V, and the short-circuit current and the transferred charge decrease (**Figure 4**a; Figure S6a–c, Supporting Information). Increasing the number of furs will effectively improve the output performance of TD-GM-TENG. When the number is 7, the transferred charge reaches 160 nC (Figure 4b; Figure S6d, Supporting Information). Under the same experimental conditions, the transferred charge during clockwise rotation is ≈70% of that during counterclockwise rotation (at 60 rpm, clockwise rotation produces 140 nC, while counterclockwise rotation produces 200 nC). As shown in Figure 4c–e, this is because the tilt angle of the fur directly changes the pressure when the fur contacts the FEP, which in turn affects the output performance of TD-GM-TENG. When the angle changes, the torque on the axis is measured separately, and it can be found that the torque increases with the increase in angle (Figure 4f). When the fur is tilted 45°, an upward normal force (F_N) and a friction force (F_f) are generated between the fur and the FEP. By applying the parallelogram rule: $F_a = \cos45° \, F_N$. At this point, the F_f experienced by fur on FEP surface can be expressed as $F_f = F \mathfrak{t} F_a$. Therefore, the force is the smallest and the output performance is the lowest when the fur is tilted at 45°. This is illustrated in Figure S7 (Supporting Information). The maximum short-circuit current is ≈5 µA, with a transferred charge of 140 nC. It is evident that with increasing speed, the transferred charge stabilizes at 40 nC. At this higher speed, the transferred charge is ≈29% of that at the lower speed. The reason for this decrease is that the contact between the fur and FEP is poorer at higher rotation speeds. When the fur is tilted 90°, F_f can be expressed as: $F_f = F$. The output performance is shown in Figure S8 (Supporting Information). The short-circuit current is 5 µA and the transferred charge is 160 nC. The output performance stabilizes at 135 nC at high speed, which is ≈84% of the value observed at low speed. When fur had a 135° inclination, its angle with FEP was 45°. The component of the supporting force F_N in the horizontal plane can be expressed as $F_a = \cos45° \, F_N$. Therefore, the frictional force acting on fur can be expressed as $F_f = F_a \mathfrak{r} F$. As illustrated in Figure S9 (Supporting Information), during counterclockwise rotation, the output performance peaked at a 135° inclination, with a short-circuit current of 9 µA and a transferred charge of 200 nC. Notably, the transferred charge at 135° was 1.43 times greater than that at 90° (Figure 4g; Figure S10, Supporting Information). Comparison of the short-circuit current at different inclinations (45°, 90°, and 135°) during counterclockwise rotation. Short-circuit current increases with the increase in rotation speed (Figure 4h).

Figure 4i shows the effect of tilt angle on the rotation speed of TD-GM-TENG with different counterweights. Under the same counterweight, an angle with smaller friction resistance can maintain a higher rotation speed. Increasing the angular momentum of TD-GM-TENG is another way to increase the rotational speed, increasing the angular momentum through springs of different lengths. As shown in Figure 4j, the rotational speed and charge transfer rate increase with the increase of spring length, and the performance reaches its peak when the spring length is 15 cm, achieving a transfer charge of 1.2 µC s^{-1}. However, a spring that is too long has little effect on the rotational speed. This is because there are gaps in the internal structure of TD-GM-TENG, which can easily cause resonance and reduce the rotational speed. After the final optimization, the power test of TD-GM-TENG at different speeds was carried out on the motor, as shown in Figure S11 (Supporting Information). The increase in rotational speed will significantly increase the peak power of TD-GM-TENG.

The output performance and practical application of TD-GM-TENG are shown in **Figure 5**. TD-GM-TENG can be used as an emergency power supply system at ocean. By distributing arrays of different sizes on the sea surface, it can provide power for various offshore platforms and self-driving equipment. For example, it can provide power for some offshore beacons and some underwater sensors, providing a wide range of application scenarios for the development of self-powered equipment and the blue economy (Figure 5a). Figure 5b shows the load output of TD-GM-TENG. This work significantly improved the charge density of TD-GM-TENG through the topological defect strategy, reaching a charge density of 90 µC m^{-2}, which is higher than other spherical structure work in recent years (Figure 5c; Table S2, Supporting Information). In the simulated wave environment, the peak power output of TD-GM-TENG reaches ≈3.7 mW when the matching resistance is 100 MΩ, as shown in Figure 5d. The power density of TD-GM-TENG is shown in Figure S12 (Supporting Information). In the face of relatively low-frequency wave energy, TD-GM-TENG also has excellent energy conversion efficiency. Under the condition of 1 Hz simulated wave, its single output energy can reach 21.43 µJ, and the output energy in 1 min can reach 31.12 mJ, with an energy conversion efficiency of 2.1% (Figure S13, Supporting Information). To assess the impact of various factors on the output performance, a correlation analysis was conducted on the transferred charge, as shown in Figure 5e. The analysis found that the optimization of the topological defect strategy has the greatest impact on the transfer charge, while the rotation angle has the smallest impact on the transfer charge. Figure 5f illustrates that TD-GM-TENG effectively captures low-frequency wave energy from various directions, with short-circuit current increasing as wave frequency rises. However, when the wave direction is the same as the electrode direction, the output performance of TD-GM-TENG decreases by ≈20%. The primary cause of the decline in electrical performance is the angle between the direction of wave motion and the direction of TENG motion. This angle shortens the acceleration phase of the TENG, thereby altering its output performance. Additionally, an increased angle induces resonance, which reduces the efficiency

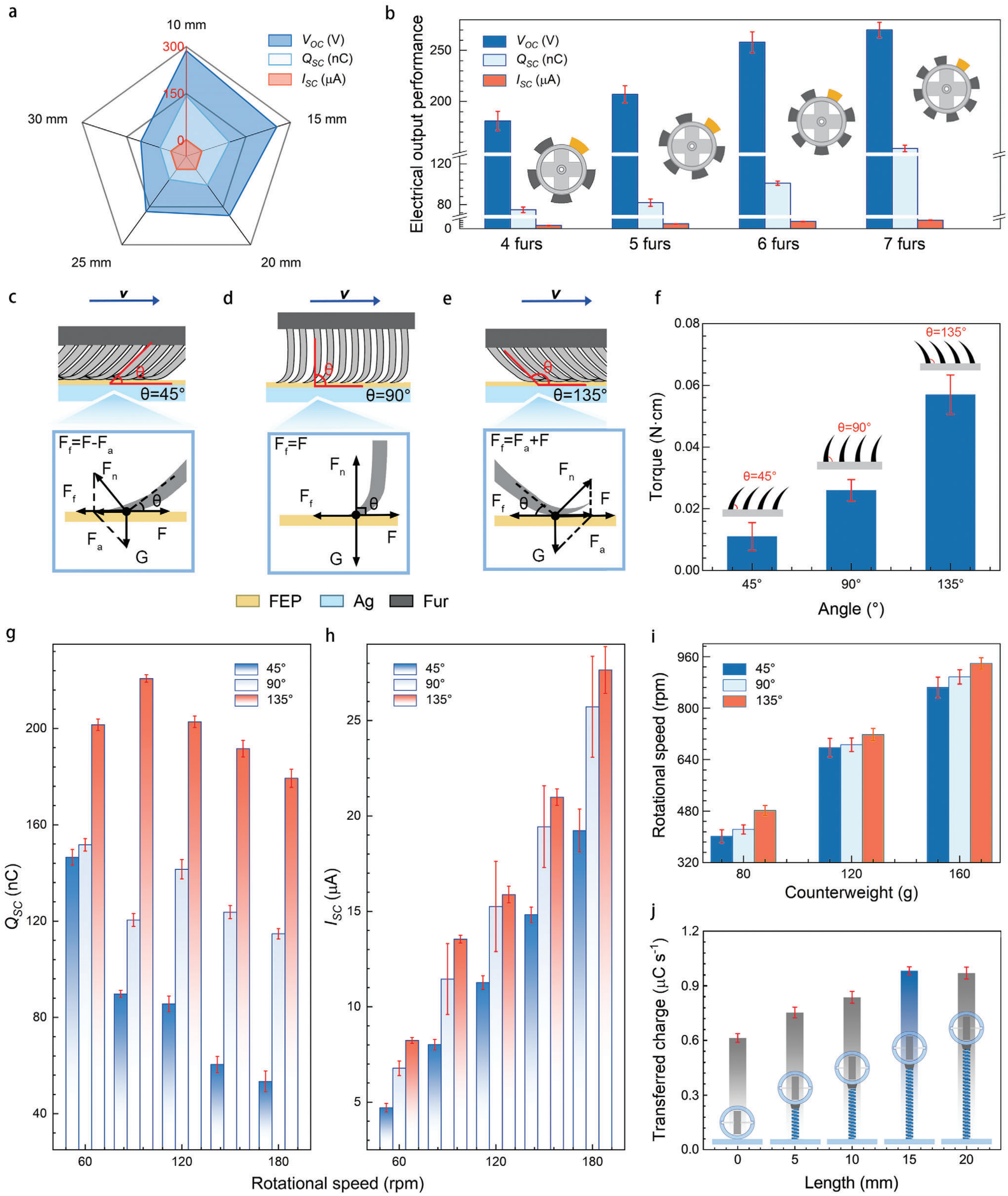

Figure 4. Electrical output performance of TD-GM-TENG with different structural parameters. a) The output performance of TD-GM-TENG with different fur lengths. b) The output performance of TD-GM-TENG with different numbers of fur. c) Schematic diagram for stress analysis of fur inclined at 45°. d) Schematic diagram for stress analysis of fur inclined at 90°. e) Schematic diagram for stress analysis of fur inclined at 135°. f) The relationship between furs tilt angle and shaft torque. g) The relationship between rotation speed and transferred charge at different fur tilt angles (45°, 90°, and 135°). h) The relationship between rotation speed and short-circuit current at different fur tilt angles (45°, 90°, and 135°). i) The relationship between the rotation speed and the counterweight at different fur tilt angles. j) The relationship between different spring lengths and transferred charge.

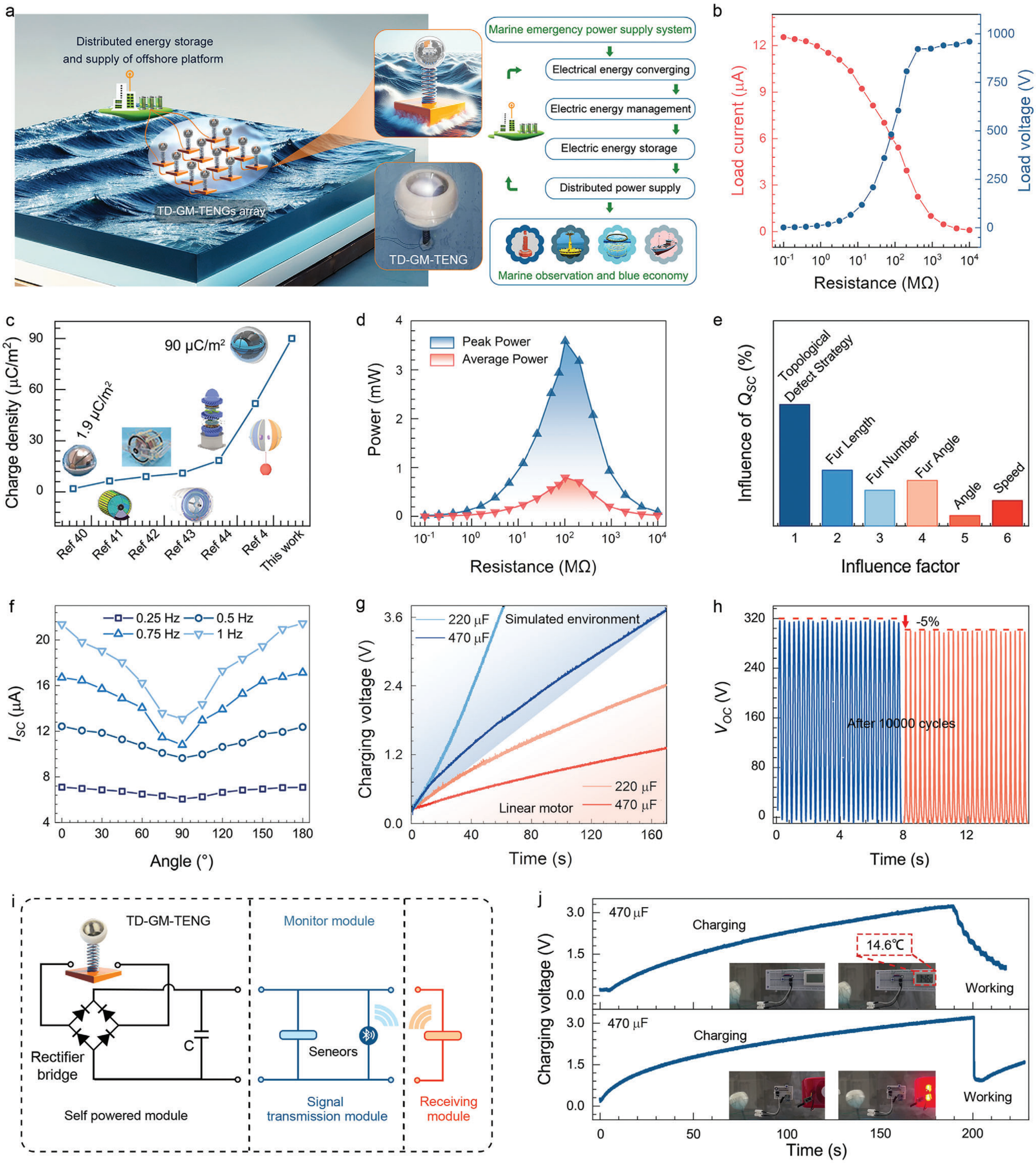

Figure 5. Application demonstration and comprehensive performance of TD-GM-TENG. a) The application scenarios of TD-GM-TENG. b) Electrical output performance of TD-GM-TENG under different load resistances. c) Comparison of charge density between this work and other works in recent years. d) Output average power and peak power of TD-GM-TENG. e) Transferred charge of TD-GM-TENG with different structural parameters. f) Relationship between water flow angle and short-circuit current of TD-GM-TENG at different water flow frequencies. g) Comparison of charging voltage of TD-GM-TENG in simulated environment and laboratory environment. h) Output stability and durability performance of TD-GM-TENG after 10 000 cycles. i) Circuit diagram of ocean emergency power supply system based on TD-GM-TENG. j) Application demonstrations of TD-GM-TENG supplies power to the alarm and thermometer with 470 μF capacitor.

of angular momentum transfer and adversely impacts the rotational speed. Given that the direction of waves in real ocean environments is inherently random, it is challenging to mitigate this phenomenon effectively. Currently, one approach to address this issue involves refining the 3D printing process to reduce gaps between the rotor, frame, and casing, thereby minimizing resonance between components and improving overall output performance. At a simulated wave of 1 Hz, TD-GM-TENG charges a 220 μF capacitor to 4 V in 80 s and a 470 μF capacitor to 4 V in 180 s. However, the charging speed tested on the motor is lower than that tested in the simulation environment. The reason is that the speed of TD-GM-TENG tested on the motor is much lower than that of TD-GM-TENG in the simulation environment (Figure 5g). The soft contact triboelectric layer used by TD-GM-TENG also greatly improves durability. In addition, the durability of the TENG system is greatly increased through measures such as packaging and keeping it away from the water surface. After 10 000 cycles of testing, the output performance dropped by ≈5% (Figure 5h). Figure 5i shows the application of TD-GM-TENG. Connecting a 470 μF capacitor in parallel with the thermometer allows the capacitor to be charged to 3.4 V within 180 s, allowing the thermometer to operate successfully after activation. Similarly, connecting a 470 μF capacitor in parallel with the siren also allows the siren to be charged to 3.4 V within 180 s (Figure 5j). In summary, these results confirm its potential as an effective blue energy harvesting solution, which is essential for supporting ocean self-powered systems.

3. Conclusion

In this paper, an innovative topological defect gyro-multi-grid triboelectric nanogenerators (TD-GM-TENGs) and their array were developed, which has demonstrated a remarkable ability to convert low-grade wave energy into electrical energy. The rotation speed of TD-GM-TENG was achieved to regulate from low to high by the precession effect. The maximum speed reached nearly 1000 rpm, and the transferred charge rate reached 3.1 μC s^{-1}. The accumulation efficiency of triboelectric charge by topological defect strategy has been improved to ≈240%. In addition, the structural parameters of the device to focus on the electrical output performance were studied and discussed. The charge density reached 90 μC m^{-2} in a cycle of 0.06 s, which is 1.6 times higher than the same kind of spherical-TENGs in the field of ocean energy harvesting. The output peak power of TD-GM-TENG unit offered 3.7 mW at the simulated water wave environment of 1 Hz. Furthermore, TD-GM-TENG was successfully used to power the thermometer and alarm and demonstrates its applicability and feasibility of being used as a distributed emergency power supply in the offshoring observation and early warning services.

4. Experimental Section

The rotor, support, shell, and other parts of TD-GM-TENG were made of 3D-printed photosensitive resin. The outer diameter of the shell was 120 mm and thickness was 18 mm. The raised 4 mm platform at the bottom of the shell was a 10 mm wide nano silver electrode and FEP layer. The diameter of the support was 106 mm, and there were two grooves at both ends to fix the one-way bearing. The diameter of the rotor was 94 mm, and there were 7 sections of fur and a section of copper electrode evenly distributed on the surface, each section was 10 mm long and 10 mm high. The rotating shaft was made of stainless steel, 107 mm long and 4 mm in diameter, with a 6 mm long and 3 mm diameter stepped structure at both ends for fixing the one-way bearing.

Assembly of TD-GM-TENG: The rotor was fixed to the center of the rotating shaft, and the one-way bearing was connected at both ends. The shaft and its bearing were then fixed to the bracket. Lead weights were added to increase its mass. The bracket was placed in the track of the shell to fix all components. Finally, the TD-GM-TENG unit was encapsulated in an acrylic shell with a diameter of 130 mm and a thickness of 5 mm.

The open circuit voltage, short circuit current, and transferred charge of TD-GM-TENG were measured using an electrostatic voltmeter (Keithley 6514), and the data were acquired in real-time through a programmed LabVIEW interface. A servo motor (Times Brilliant XK80AEA04030-SCK servo motor) and a linear motor (LinMot X12BC) provided triggering conditions for TD-GM-TENG. The electrical output was tested under simulated conventional sea wave conditions, where the blades of the wave generator were vibrated by a crankshaft driven by a servo motor. A reverse wave absorber was used in the device, whose inclined surface was covered by a porous pad. The short circuit current, open circuit voltage, transferred charge, and capacitor charging voltage were measured across various devices in a simulated environment using an electrostatic voltmeter (Keithley 6514).

Supporting Information

Supporting Information is available from the Wiley Online Library or from the author.

Acknowledgements

This work was supported by the National Key Research and Development Program of China (Grant No. 2023YFB2604600).

Conflict of Interest

The authors declare no conflict of interest.

Author Contributions

W.G. and X.G. contributed equally to this work. W.G. contributed to data curation, investigation, methodology, and the writing of the original draft. X.G. was involved in data curation and the review and editing of the manuscript. J.S. was responsible for reviewing and editing the manuscript. H.C. participated in data curation, while H.L. was responsible for the investigation. B.C. provided funding acquisition, resources, and supervision, and was also involved in the review and editing of the manuscript. Z.L.W. played a key role in the conceptualization and the review and editing of the manuscript.

Data Availability Statement

The data that support the findings of this study are available from the corresponding author upon reasonable request.

Keywords

charge accumulation, gyro-multigrid triboelectric nanogenerator, ocean emergency power supply system, topological defect, wave energy harvester

Received: November 18, 2024
Revised: December 26, 2024
Published online:

[1] L. Atzori, A. Iera, G. Morabito, *Comput. Netw.* **2010**, *54*, 2787.
[2] Y. Zi, L. Lin, J. Wang, S. Wang, J. Chen, X. Fan, P. K. Yang, F. Yi, Z. L. Wang, *Adv. Mater.* **2015**, *27*, 2340.
[3] J. Zhu, M. Zhu, Q. Shi, F. Wen, L. Liu, B. Dong, A. Haroun, Y. Yang, P. Vachon, X. Guo, *EcoMat.* **2020**, *2*, 12058.
[4] X. Zhang, Q. Yang, P. Ji, Z. Wu, Q. Li, H. Yang, X. Li, G. Zheng, Y. Xi, Z. L. Wang, *Nano Energy.* **2022**, *99*, 107362.
[5] C. Zhang, L. He, L. Zhou, O. Yang, W. Yuan, X. Wei, Y. Liu, L. Lu, J. Wang, Z. L. Wang, *Joule.* **2021**, *5*, 1613.
[6] S. Hajra, A. Ali, S. Panda, H. Song, P. M. Rajaitha, D. Dubal, A. Borras, P. In-Na, N. Vittayakorn, V. Vivekananthan, H. J. Kim, S. Divya, T. H. Oh, *Adv. Energy Mater.* **2024**, *14*, 2400025.
[7] Y. Yang, J. Wen, F. Chen, Y. Hao, X. Gao, T. Jiang, B. Chen, Z. L. Wang, *Adv. Funct. Mater.* **2022**, *32*, 2200521.
[8] J. Lee, S. Hajra, S. Panda, W. Oh, Y. Oh, H. Shin, Y. K. Mishra, H. J. Kim, *Int. J. of Precis. Eng. and Manuf.-Green Tech.* **2024**, *11*, 233.
[9] F. Xing, Z. Ou, X. Gao, B. Chen, Z. L. Wang, *Adv. Funct. Mater.* **2022**, *32*, 2205275.
[10] K. R. Kaja, S. Hajra, S. Panda, M. A. Belal, U. Pharino, H. Khanbareh, N. Vittayakorn, V. Vivekananthan, C. Bowen, H. J. Kim, *Nano Energy.* **2024**, *131*, 110319.
[11] Z. L. Wang, J. Chen, L. Lin, *Energy Environ. Sci.* **2015**, *8*, 2250.
[12] Z. L. Wang, *Mater. Today.* **2017**, *20*, 74.
[13] Z. L. Wang, *Faraday Discuss.* **2014**, *176*, 447.
[14] S. Panda, S. Hajra, Y. Oh, W. Oh, J. Lee, H. Shin, V. Vivekananthan, Y. Yang, Y. K. Mishra, H. J. Kim, *Small.* **2023**, *19*, 2300847.
[15] F. Wang, J. D. Harindintwali, Z. Yuan, M. Wang, F. Wang, S. Li, Z. Yin, L. Huang, Y. Fu, L. Li, *Innov.* **2021**, *2*, 4.
[16] L. Zu, J. Wen, S. Wang, M. Zhang, W. Sun, B. Chen, Z. L. Wang, *Sci. Adv.* **2023**, *9*, eadg5152.
[17] E. Su, H. Li, J. Zhang, Z. Xu, B. Chen, L. N. Cao, Z. L. Wang, *Adv. Funct. Mater.* **2023**, *33*, 2214934.
[18] J. A. Stankovic, *IEEE Internet of Things J.* **2014**, *1*, 3.
[19] F. Xing, X. Gao, J. Wen, H. Li, H. Liu, Z. L. Wang, B. Chen, *Adv. Sci.* **2024**, *11*, 2401076.
[20] G. Yu, J. Wen, H. Li, Y. Shang, Z. L. Wang, B. Chen, *Nano Energy.* **2024**, *119*, 109062.
[21] H. Oh, S. S. Kwak, B. Kim, E. Han, G. H. Lim, S. W. Kim, B. Lim, *Adv. Funct. Mater.* **2019**, *29*, 1904066.
[22] S. Niu, Z. L. Wang, *Nano Energy.* **2015**, *14*, 161.
[23] P. A. Lynn, *Electricity from wave and tide: an introduction to ocean energy*, John Wiley & Sons, Hoboken, NJ **2013**, pp. 3.
[24] Y. Liu, W. Yan, J. Han, B. Chen, Z. L. Wang, *Adv. Funct. Mater.* **2022**, *32*, 2202964.
[25] F. Zhang, L. Zheng, H. Li, G. Yu, S. Wang, F. Xing, Z. L. Wang, B. Chen, *Chem. Eng. J.* **2024**, *488*, 150875.
[26] H. Li, J. Wen, Z. Ou, E. Su, F. Xing, Y. Yang, Y. Sun, Z. L. Wang, B. Chen, *Adv. Funct. Mater.* **2023**, *33*, 2212207.
[27] X. Gao, F. Xing, X. Hang, F. Guo, J. Wen, W. Sun, H. Song, Z. L. Wang, B. Chen, *Chem. Eng. J.* **2024**, *493*, 152645.
[28] U. Khan, T. H. Kim, H. Ryu, W. Seung, S. W. Kim, *Adv. Mater.* **2017**, *29*, 1603544.
[29] T. Jiang, L. M. Zhang, X. Chen, C. B. Han, W. Tang, C. Zhang, L. Xu, Z. L. Wang, *ACS Nano.* **2015**, *9*, 12562.
[30] H. Liu, M. Zhang, L. Zu, J. Wen, H. Li, F. Xing, M. Yan, Z. L. Wang, B. Chen, *Nano Energy.* **2024**, *125*, 109585.
[31] Y. Hao, J. Wen, X. Gao, D. Nan, J. Pan, Y. Yang, B. Chen, Z. L. Wang, *ACS Nano.* **2022**, *16*, 1271.
[32] K. Han, J. Luo, J. Chen, B. Chen, L. Xu, Y. Feng, W. Tang, Z. L. Wang, *Microsyst. Nanoeng.* **2021**, *7*, 7.
[33] J. A. Guerrero-Ibanez, S. Zeadally, J. Contreras-Castillo, *IEEE Wirel. Commun.* **2015**, *22*, 122.
[34] X. Gao, F. Xing, F. Guo, J. Wen, H. Li, Y. Yang, B. Chen, Z. L. Wang, *Mater. Today.* **2023**, *65*, 26.
[35] X. Wang, L. Chen, Z. Xu, P. Chen, C. Ye, B. Chen, T. Jiang, Z. Hong, Z. L. Wang, *Small.* **2024**, *20*, 2310809.
[36] S. Yong, H. Wang, Z. Lin, X. Li, B. Zhu, L. Yang, W. Ding, R. Liao, J. Wang, Z. L. Wang, *Adv. Energy Mater.* **2022**, *12*, 2202469.
[37] M. Li, H.-W. Lu, S.-W. Wang, R.-P. Li, J.-Y. Chen, W.-S. Chuang, F.-S. Yang, Y.-F. Lin, C.-Y. Chen, Y.-C. Lai, *Nat. Commun.* **2022**, *13*, 938.
[38] R. H. Brandenberger, *Int. J. Mod. Phys. A.* **1994**, *9*, 2117.
[39] B. Barker, R. O'Connell, *Lett. Nuovo Cimento.* **1970**, *4*, 561.
[40] Q. Gao, Y. Xu, X. Yu, Z. Jing, T. Cheng, Z. L. Wang, *ACS Nano.* **2022**, *16*, 6781.
[41] B. Cao, P. Wang, P. Rui, X. Wei, Z. Wang, Y. Yang, X. Tu, C. Chen, Z. Wang, Z. Yang, *Adv. Energy Mater.* **2022**, *12*, 2202627.
[42] Y. Hu, H. Qiu, Q. Sun, Z. L. Wang, L. Xu, *Small Methods.* **2023**, *7*, 2300582.
[43] X. Wang, C. Ye, P. Chen, H. Pang, C. Wei, Y. Duan, T. Jiang, Z. L. Wang, *Adv. Funct. Mater.* **2024**, *34*, 2311196.
[44] S. Yang, C. Zhang, Z. Du, Y. Tu, X. Dai, Y. Huang, J. Fan, Z. Hong, T. Jiang, Z. L. Wang, *Adv. Energy Mater.* **2024**, *14*, 2304184.